Mon. Not. R. Astron. Soc. **384,** 1597–1610 (2008) doi:10.1111/j.1365-2966.2007.12808.x

The SCUBA HAlf Degree Extragalactic Survey – VI. 350-μm mapping of submillimetre galaxies

Kristen Coppin,[1,2⋆] Mark Halpern,[1] Douglas Scott,[1] Colin Borys,[3] James Dunlop,[4] Loretta Dunne,[5] Rob Ivison,[4,6] Jeff Wagg,[7,8] Itziar Aretxaga,[8] Elia Battistelli,[1] Andrew Benson,[9] Andrew Blain,[9] Scott Chapman,[9] Dave Clements,[10] Simon Dye,[11] Duncan Farrah,[12] David Hughes,[8] Tim Jenness,[13] Eelco van Kampen,[14] Cedric Lacey,[2] Angela Mortier,[4] Alexandra Pope,[1] Robert Priddey,[15] Stephen Serjeant,[16] Ian Smail,[2] Jason Stevens[15] and Mattia Vaccari[17]

[1]*Department of Physics & Astronomy, University of British Columbia, 6224 Agricultural Road, Vancouver, British Columbia, Canada V6T 1Z1*
[2]*Institute for Computational Cosmology, University of Durham, South Road, Durham DH1 3LE*
[3]*Department of Astronomy & Astrophysics, University of Toronto, 50 St George Street, Toronto, Ontario, Canada M5S 3H4*
[4]*Institute for Astronomy, University of Edinburgh, Royal Observatory, Blackford Hill, Edinburgh EH9 3HJ*
[5]*The Centre for Astronomy & Particle Theory, The School of Physics & Astronomy, University of Nottingham, University Park, Nottingham NG7 2RD*
[6]*UK ATC, Royal Observatory, Blackford Hill, Edinburgh EH9 3HJ*
[7]*National Radio Astronomy Observatory, PO Box 0, Socorro, NM 87801, USA*
[8]*Instituto Nacional de Astrofísica, Óptica y Electrónica, Apartado Postal 51 y 216, 72000 Puebla, Pue., Mexico*
[9]*Caltech, 1200 E. California Blvd, Pasadena, CA 91125-0001, USA*
[10]*Astrophysics Group, Blackett Laboratory, Imperial College, Prince Consort Road, London SW7 2BW*
[11]*School of Physics and Astronomy, Cardiff University, 5 The Parade, Cardiff CF24 3YB*
[12]*Department of Astronomy, Cornell University, Space Sciences Building, Ithaca, NY 14853, USA*
[13]*Joint Astronomy Centre, 660 N. A'ohōkū Place, University Park, Hilo, HI 96720, USA*
[14]*Institute for Astro- and Particle Physics, University of Innsbruck, Technikerstr. 25, A-6020 Innsbruck, Austria*
[15]*Centre for Astrophysics Research, Science and Technology Research Institute, University of Hertfordshire, College Lane, Hatfield, Hertfordshire AL10 9AB*
[16]*Department of Physics, The Open University, Milton Keynes MK7 6AA*
[17]*Department of Astronomy, University of Padova, Vicolo dell'Osservatorio 2, 35122 Padova, Italy*

Accepted 2007 December 4. Received 2007 December 4; in original form 2007 May 21

ABSTRACT

A follow-up survey using the Submillimetre High-Angular Resolution Camera (SHARC-II) at 350 μm has been carried out to map the regions around several 850-μm-selected sources from the Submillimetre HAlf Degree Extragalactic Survey (SHADES). These observations probe the infrared (IR) luminosities and hence star formation rates in the largest existing, most robust sample of submillimetre galaxies (SMGs). We measure 350-μm flux densities for 24 850-μm sources, seven of which are detected at $\geq 2.5\sigma$ within a 10 arcsec search radius of the 850-μm positions. When results from the literature are included the total number of 350-μm flux density constraints of SHADES SMGs is 31, with 15 detections. We fit a modified blackbody to the far-IR (FIR) photometry of each SMG, and confirm that typical SMGs are dust-rich ($M_{\rm dust} \simeq 9 \times 10^8\,{\rm M}_\odot$), luminous ($L_{\rm FIR} \simeq 2 \times 10^{12}\,{\rm L}_\odot$) star-forming galaxies with intrinsic dust temperatures of $\simeq$35 K and star formation rates of $\simeq 400\,{\rm M}_\odot\,{\rm yr}^{-1}$. We have measured the temperature distribution of SMGs and find that the underlying distribution is slightly broader than implied by the error bars, and that most SMGs are at 28 K with a few hotter. We also place new constraints on the 350-μm source counts, $N_{350}(>25\,{\rm mJy}) \sim 200$–$500\,{\rm deg}^{-2}$.

Key words: surveys – galaxies: formation – galaxies: high-redshift – galaxies: starburst – cosmology: observations – submillimetre.

⋆E-mail: kristen.coppin@durham.ac.uk

1 INTRODUCTION

The Submillimetre Common-User Bolometer Array (SCUBA) HAlf Degree Extragalactic Survey (SHADES; Mortier et al. 2005; Coppin et al. 2006) mapped $\simeq$0.25 deg^2 of sky with an rms of 2 mJy at 850 μm with SCUBA (Holland et al. 1999). The area was split approximately evenly between the Lockman Hole (LH) and the Subaru-*XMM* Deep Field (SXDF). Using uniform selection criteria, the survey uncovered 120 submillimetre galaxies (SMGs) with a median deboosted flux density of $\sim$5 mJy (Coppin et al. 2006). The SHADES programme was designed to study the nature and evolution of high star formation rate (SFR) SMGs via a systematic study of a well-characterized and statistically meaningful sample. The programme includes an effort to identify members of the source list at other wavelengths using deep follow-up data from the radio (Ivison et al. 2007) to X-ray, in order to characterize the SHADES population and to probe the variation in the star formation and clustering with redshift. The relatively precise positions available from the radio data greatly aid in identifying secure counterparts at other wavelengths, which can then be used to provide spectroscopic or photometric redshifts (Aretxaga et al. 2007) and to categorize the sources.

Even combined with knowledge of source redshift, SCUBA 850 μm and millimetre wavelength fluxes do not constrain the total dust mass of a galaxy because there is an ambiguity between column density and source temperature. The submillimetre (submm) spectral energy distribution (SED) of a luminous dusty galaxy arises from the re-emission at far-infrared (FIR) wavelengths of absorbed optical/ultraviolet radiation from regions of intense star formation (see e.g. Sanders & Mirabel 1996, and references therein). Typically the dust temperature is within a factor of 2 of $T_{\rm d} \sim 40$ K (Blain et al. 2002), so the rest-frame SED peaks in the range 60–120 μm and the SED is almost a simple power law at the SCUBA wavelengths and longer.

At a redshift of $\langle z \rangle \sim 2$ or 3, typical of SMGs (Chapman et al. 2005), the peak of the SED is shifted to be near 350 μm, and the Submillimetre High Angular Resolution Camera (SHARC-II; Dowell et al. 2003) at the Caltech Submillimetre Observatory (CSO) is very well situated to provide the photometry needed to constrain the temperatures, and therefore the luminosities and masses, of the SHADES sources.

We have therefore mapped a subset of the SHADES catalogue with SHARC-II. In this paper we constrain the FIR SEDs of our sample by fitting modified blackbody curves to the FIR photometry of 31 SHADES SMGs including SHARC-II data at 350 μm. Sections 2 and 3 describe the observations and data reduction. Section 4 presents the 350-μm flux densities of the SHADES galaxies and the FIR SEDs. Section 5 provides a discussion of the results. Conclusions and future prospects are discussed in Section 6. We adopt the cosmological parameters from the *Wilkinson Microwave Anisotropy Probe* (*WMAP*) fits in Spergel et al. (2003): $\Omega_\Lambda = 0.73$, $\Omega_{\rm m} = 0.27$ and $H_0 = 71\,{\rm km\,s^{-1}\,Mpc^{-1}}$.

2 SURVEY DESIGN AND OBSERVATIONS

2.1 Instrument description

SHARC-II is a background-limited 350- and 450-μm common-user continuum camera with a 3×1.5 arcmin^2 field of view (FOV) at the 10.4-m CSO in Hawaii (Dowell et al. 2003). The dish has a very low surface error (10.4-μm rms at 350 μm) due to the active Dish Surface Optimization System (Leong 2005) which corrects the primary for surface imperfections and gravitational deformations as a function of elevation angle during observations to improve the telescope efficiency and pointing. The result is that the CSO is probably the best telescope in the world at shorter submm wavelengths. The resulting beam size (with good focus and pointing) is 9 arcsec full width at half-maximum (FWHM) at 350 μm.

2.2 Sample selection

120 submm sources have been identified in the SHADES fields (Coppin et al. 2006). Obtaining useful photometry for the full set would require several hundred hours of excellent weather, so we have chosen to observe a carefully chosen subset of the SHADES catalogue. Many sources lie close enough together that multiple targets can be selected within a single SHARC-II FOV. We chose eight of our 14 fields to contain a large fraction of the SHADES close angular pairs. This is mostly just for efficiency, but there is also a small chance that the observations would help measure clustering in the SHADES catalogue. We chose a deliberate mixture of sources with compact, extended or no radio counterparts (Ivison et al. 2007): 11 sources with one robust compact radio ID; three sources with two robust compact radio counterparts; three sources with one extended-looking radio counterpart; and seven sources with no reliable radio ID. Choosing targets with this mixture of radio characteristics could help refine the SHADES redshift distribution and test if there is a subpopulation with a high-redshift tail (e.g. Dunlop 2001; Ivison 2006).

Two of our fields were also observed by Kovacs et al. (2006) or Laurent et al. (2006) (sources LOCK850.3, LOCK850.1 and LOCK850.41), which allows for cross-calibration and checks of systematics in observation and analysis. One field (LOCK44/45) covered two 850-μm source candidates from a preliminary SHADES catalogue which were later eliminated from the official SHADES catalogue since they were deemed likely to be spurious sources (Coppin et al. 2006). This field is not used in the ensuing analysis.

2.3 Observations

10 SHADES LH fields were mapped over the course of four superb stable weather nights in 2005 March and 2006 February ($0.035 < \tau_{225\,\rm GHz} < 0.06$). Four additional fields were observed in more marginal observing conditions. For each field data were collected in 10 min scans using a non-connecting Lissajous scan pattern with small amplitudes of typically 20 arcsec in both altitude and azimuth and a 'period' of 15–20 s. Integration times, typical weather conditions and resulting map depths of each SHARC-II field are given in Table 1.

By design, our strategy was to reach a map rms of $3\sigma \simeq 30$ mJy at 350 μm, sufficient to detect or place useful limits on an $S_{850} \sim 8$ mJy SMG with $T_{\rm d} \simeq 40$ K at $z \lesssim 3$. Good weather is scarce, and it is important to be as efficient as possible by only integrating down to the planned noise level. We tracked the effective integrating time on each source by compensating each 10-min file for zenith angle and atmospheric opacity at 350 μm, as inferred from the $\tau_{350\,\mu\rm m}$ and $\tau_{225\,\rm GHz}$ dippers. See Appendix A for details. Typically, 3–4 h of observations were required for a map 3×1.5 arcmin^2 in size.

Pointing, focus checks and calibration were performed hourly on standard sources in close proximity to the science targets. The same scan pattern was used as for the science targets, but with integration times of only 120–160 s (as typical flux densities are $\gtrsim$2 Jy).

Table 1. Summary of the SHARC-II observations and map properties. RA and Dec. (J2000) coordinates are given for the field pointing centre, with each field containing one or more SHADES sources. The date of observations, weather conditions (mean atmospheric opacity at 350 μm), and the 'effective' integration times (see Appendix A; note that this is not the same as the actual time spent on the sky) are listed. Since a large fraction of each map comprises noisy edges, we quote a median value of a 'trimmed' noise map containing only pixels with more than 60 per cent of the maximum depth coverage achieved by the central pixel in the map. Total map areas are also given.

Field name	SHADES sources	RA (J2000)	Dec. (J2000)	UT date (yy-mm-dd)	Mean $\tau_{350\,\mu m}$	Effective integration time (min)	Median rms (mJy)	Map area (arcmin^2)
LOCK21/28	21, 28	$10^h52^m57^s.3$	$57°30'54''.0$	05-02-28/-03-08,09	1.30	8.5	13	3.1
LOCK26/32	26	$10^h52^m39^s.7$	$57°23'16''.4$	05-02-28	0.99	9.3	9	3.1
LOCK4/69	4	$10^h52^m05^s.5$	$57°27'06''.4$	05-02-28	0.88	9.9	10	3.1
LOCK3/47	3, 47	$10^h52^m37^s.1$	$57°24'57''.5$	05-02-28	0.88	1.1	20	3.0
LOCK33/42	33, 77	$10^h51^m56^s.5$	$57°23'05''.5$	05-03-01	0.90	8.9	9	3.1
LOCK10/48/64	10, 48, 64	$10^h52^m52^s.0$	$57°32'51''.4$	05-03-01	0.89	9.8	13	3.7
LOCK1/41/63	1, 6, 41, 63	$10^h51^m57^s.9$	$57°24'60''.6$	05-03-01	0.80	13.7	23	3.9
LOCK16/50	16	$10^h51^m49^s.3$	$57°26'44''.5$	05-03-08	1.33	7.5	17	3.8
LOCK22/25	22	$10^h51^m35^s.2$	$57°33'26''.9$	05-03-08,09	1.52	6.0	17	3.5
LOCK44/45	none	$10^h51^m56^s.8$	$57°28'37''.9$	05-03-09	1.33	4.7	22	3.8
LOCK15	15	$10^h53^m19^s.1$	$57°21'10''.5$	06-02-24	1.52	1.1	55	2.8
SXDF1/11	1, 11	$02^h17^m27^s.9$	$-04°59'38''.0$	04-08-30,31/-09-01	1.83	6.4	14	3.8
SXDF3/8	3, 8	$02^h17^m43^s.2$	$-04°56'12''.5$	04-08-30,31/-09-01	1.81	5.2	15	4.3
SXDF17/26	17, 119	$02^h17^m55^s.8$	$-04°52'50''.4$	05-03-01,03,05,07,08,09	1.39	6.8	17	3.1

The typical pointing rms of 2–3 arcsec at the CSO is a non-negligible fraction of the 9 arcsec beam size, and much care is taken to minimize pointing errors. Observations of point-like galaxies, quasars, protostellar sources, H II regions and evolved stars are used by the CSO staff for constructing a pointing model. The model predictions for the calibrators observed before and after science observations are compared to the actual pointing measurements; offsets are calculated and applied to the model pointing predictions for the science observations during the map co-addition stage of the reduction. This procedure yields a pointing accuracy rms of ∼2 arcsec (D. Dowell, private communication).

Flux calibration is performed by comparing the known and measured flux densities and beam sizes obtained for standard calibration sources. For sources in the SXDF, oCeti (a Mira variable) and occasionally OH231 (a protoplanetary nebula) were used as pointing and calibration sources. For sources in the LH, CIT6 (an evolved star) was used, and the nearby asteroids Pallas and Egeria when CIT6 was unavailable. The standards have well-tabulated 350-μm flux densities, which are available from the CSO/SHARC-II calibration web page.[1] The final calibration is expected to be better than 15 per cent, with systematic effects being negligible at that level (CSO staff, private communication).

3 DATA REDUCTION

3.1 Mapmaking and source extraction

We make maps from the raw data and then extract 350-μm fluxes from the maps.

The mapmaking data reduction package is CRUSH (Comprehensive Reduction Utility for SHARC-II), a JAVA-based tool developed by Kovacs (2006). The software iterates a least-squares algorithm to solve for celestial emission along with instrumental and atmospheric contributions to the total power signal. CRUSH accesses the $\tau_{350\,\mu m}$ polynomial fits to obtain a low-noise 350-μm sky opacity-based estimate of the atmospheric signal. Using the 'deep' utility, as is recommended for sources fainter than 100 mJy, the maps of each field are co-added on a grid of 1.62×1.62 arcsec^2 pixels. The outer four rows of pixels are removed automatically by CRUSH since they are not sampled sufficiently well to converge to useful measurements. The data are fitted with a single Gaussian beam profile with a FWHM of 9 arcsec. Thumbnails of the reduced maps centred on the SHADES 850-μm positions are shown in Fig. 1. The bulk of the structure in these images is detector noise.

3.2 Tests of the data

Peaks are identified in maps of the signal-to-noise ratio (S/N) using an algorithm which only accepts sources separated by at least $3\sigma_{beam} = 11.5$ arcsec. The maps are also inverted and negative sources are extracted in the same way as for the positive map. The number of peaks found above a given threshold are listed in Table 2, as are the number of peaks expected in a Gaussian field. The total area of the maps searched for peaks is 44.5 arcmin^2.

Note that there are more negative peaks detected at any given noise level than are expected under the assumption that the variance is what one calculates from the time stream. However, if the maps have Gaussian distributed noise, but with a variance 7 per cent larger than we infer from the time-series the *negative* and *Gaussian* columns in Table 2 would match; the number of Gaussian peaks expected at $S/N = 0.93 \times (2, 2.5, 3)$ is (67.0, 25.0, 6.3). We find this level of agreement between variance in the time-series and variance in the maps encouraging, and use the number of negative peaks to set the statistical significance of any detections of positive flux in the maps.

3.3 350-μm flux densities of SHARC-II-detected SMGs

If a statistically significant peak is found in the SHARC-II map within a small search radius (discussed below) of a SHADES position, we infer that this is the counterpart source and can use its flux, after deboosting as per Coppin et al. (2005), to constrain the source SED.

[1] http://www.submm.caltech.edu/∼sharc.

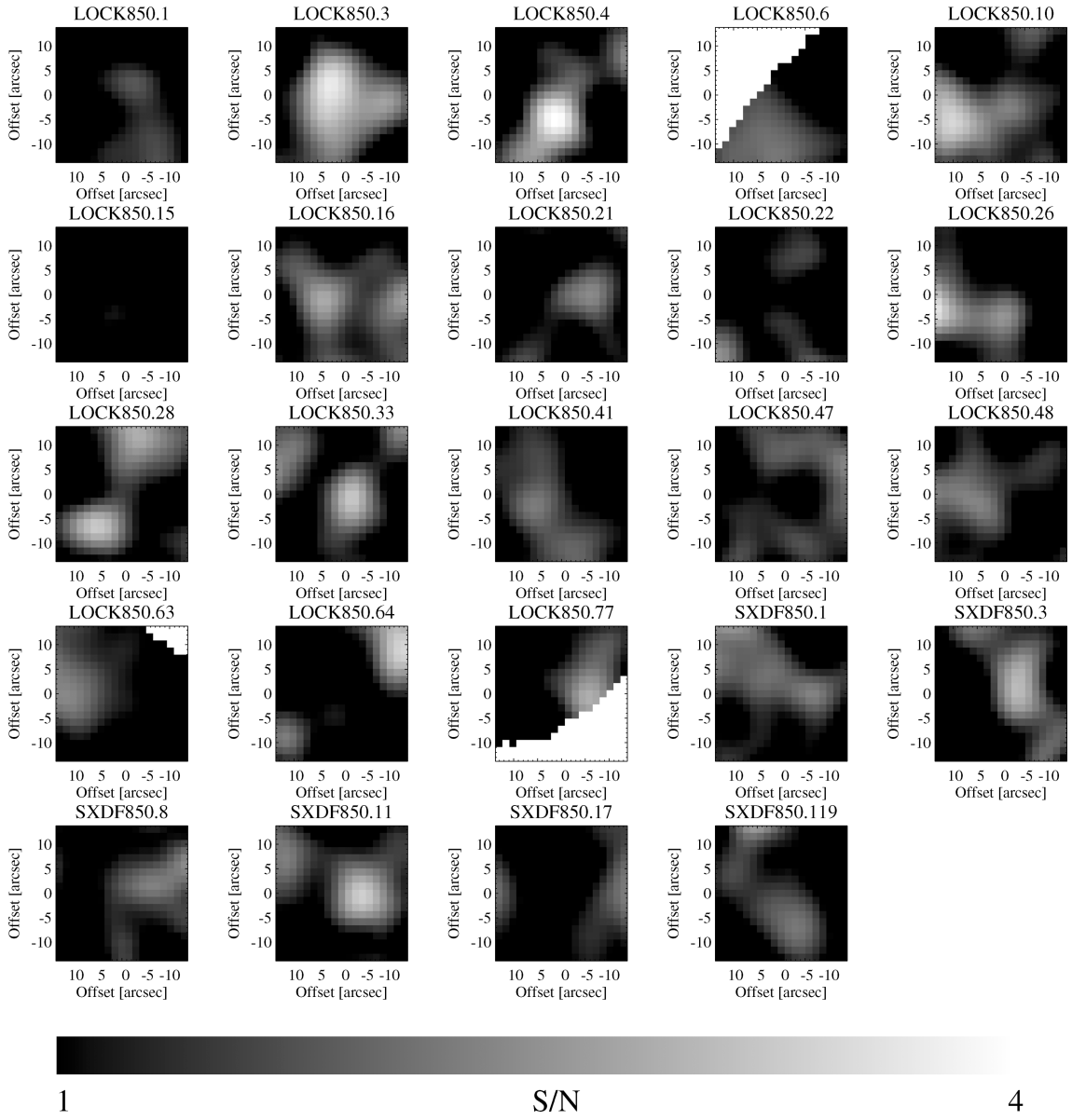

Figure 1. $30 \times 30\,\mathrm{arcsec}^2$ SHARC-II 350-μm thumbnail images of each SHADES source, centred on the 850-μm positions and using $1.62 \times 1.62\,\mathrm{arcsec}^2$ pixels. Each thumbnail is extracted from a map that has been convolved with the FWHM = 9 arcsec SHARC-II point spread function. The images are all displayed on the same flux density scale for comparison. LOCK850.6, 63 and 77 lie on the map edges. See Table 3 for the corresponding flux densities, noise estimates, S/N values and counterpart associations.

Table 2. Number of positive and negative peaks in S/N maps.

	2σ	2.5σ	3σ	4σ
Positive peaks	72	32	9	1
Negative peaks	66	28	7	0
P_{N}(10 arcsec)	12.9 per cent	5.4 per cent	1.4 per cent	–
Gaussian model	51	16	3.4	0.6
P_{N}(10 arcsec)	10.0 per cent	3.1 per cent	0.7 per cent	–

There are several different approaches to estimating the 350-μm flux density associated with SHADES sources if a SHARC-II source is *not* detected, and they are biased in different ways. (1) Measuring the flux density of each object at the 850-μm position will be biased low on average because of the uncertainty in the true source location due to the large beam size and modest S/N in the SHADES maps. (2) Measuring the flux density of the brightest pixel within a given radius of the 850-μm position will be biased slightly high on average[2] (e.g. Coppin et al. 2005; see discussion below). (3) Measuring the 350-μm flux density of each object at the precise radio position, if one exists, is less biased on average than methods 1 and 2 because of the small positional uncertainty.

Not all of the 850-μm sources mapped at 350 μm have radio counterparts. We therefore choose to measure the flux densities using method 2 and to correct for flux-boosting effects, since this

[2] Kovacs et al. (2006) and Laurent et al. (2006) adopt this approach for measuring fluxes for detections and non-detections alike.

Table 3. SHARC-II 350-μm flux densities of 850-μm sources from SHADES. Coordinates are only given for ≥2.5σ SHARC-II detections ≤10 arcsec away from the SHADES 850-μm position. Each offset has an uncertainty of about ±2 arcsec, reflecting the uncertainty in the SHARC-II map astrometry due to the rms pointing uncertainty. The flux densities in the 'brightest pixel' column represent the highest S/N pixel in the beam-convolved image within 10 arcsec of the SHADES catalogue position – these fluxes are used in the SED fitting once a correction has been made for flux-boosting (see Table 4 for the corrected fluxes). Non-detections are given in parentheses; measurements were also made on the SHARC-II maps at the SHADES 850 μm and radio positions for comparison. See the text for a discussion of the biases of each of these measurements. The observations for LOCK850.15 are insufficiently deep (incomplete) and its map is thus left out of the general analysis (see text).

SHADES ID	350-μm position		Offset	S_{350}			Comments
	RA (J2000)	Dec. (J2000)	(arcsec)	Brightest pixel (≤ 10 arcsec) (mJy)	At 850-μm position (mJy)	At radio position (mJy)	
LOCK850.01	–	–	(≃4.3)	(23.0 ± 21.2)	12.7 ± 22.2	22.6 ± 21.4	See Laurent et al. (2006)
LOCK850.03	$10^h52^m38\overset{s}{.}70$	57°24′37″.4	3.7	67.1 ± 18.5 (3.6σ)	59.7 ± 18.0	65.0 ± 18.2 58.2 ± 18.0	See Kovacs et al. (2006)
LOCK850.04	$10^h52^m04\overset{s}{.}42$	57°26′54″.3	5.0	37.3 ± 9.1 (4.1σ)	21.0 ± 9.2	18.9 ± 9.3 33.2 ± 9.1	
LOCK850.06	–	–	(≃10)	(57.0 ± 37.6)	1.8 ± 43.1	23.6 ± 39.1	Edge of SHARC-II map
LOCK850.10	–	–	(≃10)	(36.2 ± 12.0)	14.9 ± 11.9	19.4 ± 12.2	
LOCK850.15	–	–	(≃4.2)	(9.8 ± 55.7)	−32.7 ± 53.7	−8.3 ± 52.5 6.9 ± 54.9	Incomplete observations
LOCK850.16	–	–	(≃4.9)	(38.6 ± 15.8)	26.6 ± 15.5	33.3 ± 15.6	
LOCK850.21	–	–	(≃6.5)	(25.1 ± 13.2)	14.3 ± 12.9	–	
LOCK850.22	–	–	(≃10)	(13.1 ± 15.6)	−1.3 ± 15.6	–	
LOCK850.26	–	–	(≃4.5)	(18.3 ± 8.8)	6.9 ± 8.5	13.4 ± 8.6	
LOCK850.28	$10^h52^m57\overset{s}{.}86$	57°30′59″.7	10.0	34.9 ± 11.7 (3.0σ)	8.3 ± 11.8	(29.6 ± 11.6)	
LOCK850.33	$10^h51^m55\overset{s}{.}82$	57°23′11″.3	1.4	24.7 ± 8.4 (2.9σ)	21.5 ± 8.4	20.4 ± 8.4	
LOCK850.41	–	–	(≃7.5)	(42.5 ± 25.4)	15.9 ± 24.4	12.4 ± 24.2 34.8 ± 24.8	See Laurent et al. (2006)
LOCK850.47	–	–	(≃9.4)	(24.4 ± 20.9)	−8.3 ± 21.2	–	
LOCK850.48	–	–	(≃6.5)	(24.3 ± 13.5)	9.9 ± 12.3	–	
LOCK850.63	–	–	(≃10)	(52.3 ± 29.1)	9.9 ± 31.4	15.6 ± 29.1	
LOCK850.64	–	–	(≃10)	(17.4 ± 12.4)	−5.1 ± 12.8	–	
LOCK850.77	$10^h51^m56\overset{s}{.}22$	57°22′09″.8	6.3	62.1 ± 24.6 (2.5σ)	9.9 ± 18.7	−0.2 ± 17.9	Edge of SHARC-II map
SXDF850.1	–	–	(≃6.2)	(24.5 ± 13.9)	15.9 ± 14.5	15.9 ± 14.6	
SXDF850.3	$02^h17^m41\overset{s}{.}95$	−04°56′26″.3	3.4	39.3 ± 14.3 (2.7σ)	23.1 ± 14.1	23.1 ± 14.1	
SXDF850.8	–	–	(≃6.3)	(24.5 ± 14.1)	10.5 ± 14.1	18.1 ± 14.5	
SXDF850.11	$02^h17^m24\overset{s}{.}81$	−04°59′37″.2	4.6	46.6 ± 15.0 (3.1σ)	26.6 ± 14.2	22.2 ± 14.1	
SXDF850.17	–	–	(≃10)	(18.6 ± 21.0)	−13.0 ± 17.3	–	
SXDF850.119	–	–	(≃7.6)	(23.8 ± 14.9)	13.0 ± 15.3	0.8 ± 15.4	

measurement can be performed for all of our target SMGs in a uniform way. Detections, and measurements from methods 1, 2 and 3 are given in Table 3, without deboosting, for completeness and intercomparison. The deboosted fluxes are listed in Table 4. In fact we deboost the detected sources and the other sources in the same way.

The first step in either source detection or method 2 is to choose a search radius for companion sources. Too large a radius increases the false detection rate and the flux-boosting factor. Too small a radius causes sources to be missed. The rows labelled P_N(10 arcsec) in Table 2 show the percentage chance that an arbitrary 10 arcsec circle contains a peak. Using the negative peaks as a reliable measurement of the noise level in the maps, we infer that a 2.5σ peak found within 10 arcsec of a SHADES location is 5 per cent likely to be a false positive association, i.e. a 2.5σ peak found within a 10 arcsec radius is a 95 per cent confidence detection.

We use Monte Carlo techniques on the actual data to test the number of false identifications made. An area with a 10 arcsec radius around each 850-μm source is masked out so that any real counterpart will not contaminate the test. We select a random position on each map and search for a peak in the map within the given search radius above the designated S/N threshold. This is repeated 10 000 times over the SHARC-II maps, and we find that using a search radius of ≃10 arcsec and S/N $\gtrsim$ 2.5 finds a SHARC-II peak *at random* in 5 per cent of the trials, confirming the conclusion above from Table 2. We therefore adopt counterpart search criteria of 2.5σ and 10 arcsec.

We can estimate the fraction of sources for which a 10 arcsec search misses the true companion due to positional uncertainty in both the SHADES and SHARC-II data. Ivison et al. (2007) find a one-dimensional positional uncertainty of 3.2 arcsec for SHADES SMGs by comparing the 850 μm determined positions (beam FWHM = 14.8 arcsec) with more precise radio positions (synthesized beam FWHM = 1.3 arcsec). This is consistent with the theoretical expectation (see equation 2 of appendix B in Ivison et al. 2007) of $\sigma \simeq 0.6\,(\mathrm{S/N})^{-1}$ FWHM $\simeq$ 3 for FWHM = 14.8 arcsec and S/N $\simeq$ 3. The positional uncertainty of SHARC-II observations stems from the telescope pointing uncertainty, typically 2–3 arcsec. Adding these uncertainties in quadrature and converting one-dimensional uncertainties to two dimensions and then a radial distance, we expect the true 350-μm counterpart to lie within a 10 arcsec circle 93 per cent of the time. Using a larger search radius would increase the level of flux-boosting without including more sources. Peaks in the SHARC-II map will be displaced from the true

Table 4. Multiwavelength photometry of SHARC-II-observed SHADES sources. The first set are SHADES sources that use 350-μm flux densities measured here, and the second set are 350-μm flux densities of SHADES sources obtained from the literature (Kovacs et al. 2006 and Laurent et al. 2006). 350-μm photometry has been corrected for flux boosting (see Section 3.6). 850-μm (deboosted) and 450-μm photometry are from Coppin et al. (2006), 1.4-GHz and 24-μm data are from Ivison et al. (2007) ('tent.' refers to tentative identifications), 1.1- and 1.2-mm photometry are from Laurent et al. (2005) and Dunlop (private communication; an improved reduction of the Greve et al. 2004 MAMBO data), respectively. In cases where two robust radio and/or 24-μm IDs exist for a single SHADES source, both are listed. Photometric redshifts are from tables 3–5 of Aretxaga et al. (2007) and spectroscopic redshifts are from (1) Chapman et al. (2005), (2) Ivison et al. (2005), (3) Chapman et al. (2003), (4) Chapman et al. (2002).

SHADES ID	S_{350} (mJy)	S_{850} (mJy)	S_{450} (μJy)	$S_{1.4\,\mathrm{GHz}}$ (μJy)	S_{24} (mJy)	$S_{1.1\,\mathrm{mm}}$ (mJy)	$S_{1.2\,\mathrm{mm}}$	phot z	spec z
LOCK850.04	24.9 ± 9.1	$10.65\ (\pm^{1.7}_{1.8})$	<134	32.0 ± 5.1	261 ± 73	–	3.7 ± 0.4	$1.6\ (\pm^{0.3}_{0.1})$	$(0.526\,\mathrm{or}\,1.482)^2$
				73.0 ± 5.0	179 ± 68				
LOCK850.06	38.0 ± 37.6	$6.85\ (\pm^{1.3}_{1.3})$	<77	15.0 ± 4.8 (tent.)	75.1 ± 12.7	–	–	$3.6\ (\pm^{1.0}_{0.1})$	–
LOCK850.10	24.1 ± 12.0	$9.15\ (\pm^{2.7}_{2.9})$	<365	25.5 ± 6.3	–	–	–	$3.1\ (\pm^{0.9}_{0.3})$	–
LOCK850.15	6.5 ± 55.7	$13.25\ (\pm^{4.3}_{5.0})$	<149	43.9 ± 7.8	353 ± 20	–	4.1 ± 0.7	$2.4\ (\pm^{0.4}_{0.4})$	–
				61.5 ± 7.6					
LOCK850.16	25.7 ± 15.8	$5.85\ (\pm^{1.8}_{1.9})$	<67	106.0 ± 6.0	314 ± 24	–	1.8 ± 0.5	$1.9\ (\pm^{0.4}_{0.1})$	1.147^2
LOCK850.21	16.7 ± 13.2	$4.15\ (\pm^{2.0}_{2.5})$	<70	$5\sigma < 30$	97.9 ± 14.1	–	1.6 ± 0.4	≥ 1.0	–
LOCK850.22	8.7 ± 15.6	$7.55\ (\pm^{3.2}_{4.2})$	<76	$5\sigma < 30$	402 ± 21	–	–	≥ 2.0	–
LOCK850.26	12.2 ± 8.8	$5.85\ (\pm^{2.4}_{2.9})$	<48	31.4 ± 5.2	195 ± 16	–	–	$3.6\ (\pm^{0.1}_{0.8})$	–
LOCK850.28	23.3 ± 11.7	$6.45\ (\pm^{1.7}_{1.8})$	<56	–	–	–	–	≥ 2.0	–
LOCK850.33	16.5 ± 8.4	$3.85\ (\pm^{1.0}_{1.1})$	<49	51.0 ± 4.3	–	–	2.8 ± 0.6	$3.6\ (\pm^{0.7}_{0.9})$	2.664^2, 2.686^1, 3.699^3
LOCK850.47	16.3 ± 20.9	$3.55\ (\pm^{1.7}_{2.1})$	<21	–	–	–	–	≥ 1.5	–
LOCK850.48	16.2 ± 13.5	$5.45\ (\pm^{2.1}_{2.5})$	<79	–	203 ± 17	–	1.6 ± 0.4	$2.4\ (\pm^{0.5}_{0.1})$	–
LOCK850.63	34.9 ± 29.1	$3.65\ (\pm^{1.2}_{1.3})$	<50	22.6 ± 4.8	236 ± 17	–	–	$2.6\ (\pm^{0.4}_{0.4})$	–
LOCK850.64	11.6 ± 12.4	$5.85\ (\pm^{2.5}_{3.2})$	<95	–	–	–	1.7 ± 0.4	≥ 1.5	–
LOCK850.77	41.4 ± 24.6	$3.25\ (\pm^{1.2}_{1.3})$	<39	15.5 ± 4.4 (tent.)	51.7 ± 13.1	–	–	$2.6\ (\pm^{0.8}_{0.1})$	–
SXDF850.1	16.3 ± 13.9	$10.45\ (\pm^{1.5}_{1.4})$	<65	54.3 ± 9.7	–	–	–	$2.6\ (\pm^{0.4}_{0.3})$	–
SXDF850.3	26.2 ± 14.3	$8.75\ (\pm^{1.5}_{1.6})$	<81	77.2 ± 9.3	no ID	–	–	$2.1\ (\pm^{0.3}_{0.1})$	–
SXDF850.8	16.3 ± 14.1	$6.05\ (\pm^{1.8}_{1.9})$	<45	52.0 ± 9.5	–	–	–	$2.6\ (\pm^{1.3}_{0.1})$	–
SXDF850.11	31.1 ± 15.0	$4.55\ (\pm^{1.9}_{2.2})$	<79	56.8 ± 10.0	195 ± 47	–	–	$2.4\ (\pm^{0.4}_{0.4})$	–
SXDF850.17	12.4 ± 21.0	$7.65\ (\pm^{1.7}_{1.7})$	<71	–	–	–	–	≥ 2.0	–
SXDF850.119	15.9 ± 14.9	$4.55\ (\pm^{2.1}_{2.5})$	<70	38.0 ± 9.7 (tent.)	784 ± 47	–	–	$2.1\ (\pm^{0.1}_{0.1})$	–
					275 ± 47				
LOCK850.01	24.1 ± 5.5	$8.85\ (\pm^{1.0}_{1.0})$	<47	78.9 ± 4.7	217 ± 16	4.4 ± 1.3	3.6 ± 0.5	$2.4\ (\pm^{1.1}_{0.2})$	$2.148^{1,2}$
LOCK850.02	25.3 ± 10.3	$13.45\ (\pm^{2.1}_{2.1})$	<123	40.7 ± 5.6	545 ± 31	6.8 ± 1.4	5.7 ± 1.0	$2.9\ (\pm^{0.3}_{0.1})$	–
				52.4 ± 5.6				$2.9\ (\pm^{0.7}_{0.1})$	
LOCK850.03	40.5 ± 6.5	$10.95\ (\pm^{1.8}_{1.9})$	<34	35.0 ± 5.2	183 ± 33	4.8 ± 1.3	4.6 ± 0.4	$2.6\ (\pm^{0.3}_{0.1})$	$(2.94\,\mathrm{or}\,3.036^1)^2$
				25.8 ± 4.9	175 ± 23				
LOCK850.12	29.3 ± 16.0	$6.15\ (\pm^{1.7}_{1.7})$	<35	44.3 ± 5.1	263 ± 19	4.1 ± 1.3	2.6 ± 0.4	$2.6\ (\pm^{0.2}_{0.1})$	$2.142^{1,2}$
LOCK850.14	41.0 ± 6.8	$7.25\ (\pm^{1.8}_{1.9})$	<96	–	–	5.1 ± 1.3	3.4 ± 0.6	$2.6\ (\pm^{0.8}_{0.1})$	$2.611^{1,2,3}$
LOCK850.18	7.5 ± 6.7	$6.05\ (\pm^{1.9}_{2.1})$	<84	29.4 ± 4.4	–	5.1 ± 1.3	3.4 ± 0.6	$3.1\ (\pm^{2.9}_{0.1})$	$1.956^{1,2}$
LOCK850.27	3.4 ± 5.1	$5.05\ (\pm^{1.3}_{1.3})$	<32	–	–	5.2 ± 1.4	3.2 ± 0.7	$4.6\ (\pm^{1.4}_{0.4})$	–
LOCK850.30	38.0 ± 7.2	$4.75\ (\pm^{1.5}_{1.6})$	<86	245 ± 13	233 ± 19	–	(0.4 ± 0.8)	$2.1\ (\pm^{0.1}_{0.4})$	$2.689^{1,3}$
LOCK850.41	10.3 ± 5.5	$3.85\ (\pm^{0.9}_{1.0})$	<16	43.6 ± 4.7	651 ± 46	4.0 ± 1.3	2.4 ± 0.5	$3.4\ (\pm^{0.7}_{0.2})$	$0.689^{1,2,4}$
				22.1 ± 4.8	475 ± 37				
LOCK850.76	4.4 ± 6.7	$4.75\ (\pm^{2.5}_{3.1})$	<90	48.0 ± 6.0	592 ± 26	4.4 ± 1.4	–	$4.6\ (\pm^{1.4}_{1.1})$	–

counterpart location by a distance that scales with the SHARC-II beam size (9 arcsec) and the S/N ($\geq 2.5\sigma$), as for SHADES. Adding this term, we find that 90 per cent of apparent peaks associated with a counterpart will lie within our chosen 10 arcsec circle.

Proper correction for the flux boosting that results from picking off peaks in low-S/N data requires knowledge of the source count distribution (e.g. Coppin et al. 2005). However, prior information about the 350-μm source counts is not yet sufficiently well constrained. We have estimated the flux-boosting effect on this sample of low-S/N 350-μm-detected and non-detected SMGs ($\lesssim 4\sigma$) by calculating the error-weighted mean excess flux of method 2 compared to method 3 to be a factor of $\simeq 1.5$. We therefore divide each 350-μm flux measurement from method 2 (or from modest S/N detections), by 1.5 and present the deboosted fluxes in Table 4 for

use in fitting SEDs. For the highest S/N 350-μm-detected SMGs ($\gtrsim$4.5σ; Kovacs et al. 2006), flux-boosting effects are negligible and so we do not correct these fluxes.

3.4 Discussion of other 350-μm photometry of 850-μm SHADES sources

The 350-μm flux densities have been constrained for 25 per cent of the SHADES 850-μm sources, with the current work providing 21/31 of the SHADES 350-μm flux density constraints. Complementary SHARC-II observations of SMGs including several SHADES sources have been performed by Laurent et al. (2006) and Kovacs et al. (2006). Since we include their photometry in the SED fits of seven SHADES sources, it is worth describing how fluxes are measured by these groups.

Kovacs et al. (2006) conducted follow-up observations of bright (>5 mJy) radio-identified SCUBA sources with optical spectroscopic redshifts, including LOCK850.3, LOCK850.14, LOCK850.18 and LOCK850.30. They detected 12/15 of their sample with a mean S/N $\simeq$ 4.5 for the detections.

Laurent et al. (2006) performed follow-up observations of 17 Bolocam 1.1-mm-selected source candidates in the LH with SHARC-II. Of the 17, 10 are detected, including LOCK850.1, LOCK850.2, LOCK850.3, LOCK850.12, LOCK850.14, LOCK850.41, LOCK850.27 and LOCK850.76[3] (see Laurent et al. 2005 for counterpart identifications[4]).

Kovacs et al. (2006) and Laurent et al. (2006) quote as a flux the peak flux density in a specified search radius around their target source position, which is taken from either radio or mm data. They do not deboost these fluxes, but their observations are at lower noise levels so this step is less important.

Three SHADES sources that we observe in this programme, LOCK850.1, LOCK850.3 and LOCK850.41 have also been observed by Kovacs et al. (2006) and Laurent et al. (2006). Because their observations are at lower noise we use their fluxes in Table 4 and in subsequent analysis.

3.5 Formally detected 350-μm counterparts

In the analysis section of this paper we use our best estimates of the 350-μm flux of each source as photometric constraints. However, for comparison to blank field surveys it is useful to consider how many of the sources are seen at a high enough S/N that they would be counted as detections.

We have identified seven 350-μm counterparts of 850-μm sources, as presented in Table 3. The positional offsets of the detections from the SHADES positions are consistent with the positional distribution discussed above; 5/7 (71 per cent) of the detections lie within 5 arcsec. No trend is seen of decreasing positional offset with increasing S/N ratio of the seven associations, but this is not surprising given the low number statistics and the small dynamic range in S/N.

It is striking that the number of *detected* counterparts to SHADES sources exactly matches the excess of positive peaks over noise (or negative peaks) in the full mapped area, as listed in Table 2.

As we did with the number of peaks, we can use the corresponding composite negative catalogue to test if real associations are being found or just noisy peaks in the 350-μm maps. Counterparts to 850-μm sources are searched for in an inverted map in the same way, using an S/N threshold of 2.5 and search radius of 10 arcsec and no 'negative' counterparts are identified. This result reassures us that the 350-/850-μm associations are likely to be real.

3.6 350-μm flux density constraints of SMGs not individually detected by SHARC-II

Any of the following mechanisms might cause an SMG not to be detected at 350 μm. (1) The 850-μm source could be intrinsically less luminous, colder and/or have a different SED shape than the strongly detected sources. (2) The SMG could lie at a redshift in excess of about 3, this being more likely if there is also no radio counterpart, since the existing radio data are sufficiently deep to obtain a large fraction of counterparts for SMGs only for $z \lesssim 3$ (see Ivison et al. 2005). Above $z \sim 3$, the 350-μm band is sampling the Wien side of the SED and suffers from cosmological dimming without the benefit of the negative *K*-correction. (3) The SMG could be spurious, although the false positive rate in the SHADES catalogue is believed to be very low. The catalogue was carefully constructed from a comparison of multiple data reductions in order to minimize false detections (see Coppin et al. 2006).

We rely on the photometric fluxes even for the 16 sources which are not detected at high significance. Therefore we have performed a stacking analysis to determine if a significantly positive 350-μm flux density is associated with those sources. 350-μm flux densities and errors are measured on the SHARC-II maps at the radio position for 11 of these 16 sources which have a radio counterpart and we find a mean flux of 16.7 $\pm$ 4.8 mJy. This is our least biased flux estimator, and the agreement with our listed deboosted fluxes is very encouraging. The weighted mean deboosted flux for all 16 of these low significance sources is 16.6 $\pm$ 3.8 mJy.

3.7 Serendipitous 350-μm blank-field SMGs

We identify one serendipitous 3.9σ 350-μm source in our map of LOCK26/32: LOCK350.1. LOCK350.1 is not associated with any 850-μm sources, since it is $\gtrsim$15 arcsec away from any of the SHADES 850-μm positions in the map. Based on Gaussian noise statistics and the number of independent beam sizes in the survey area with noise less than 20 mJy,[5] about 0.1 false positives are expected on average at a S/N of 3.9; LOCK350.1 is therefore likely a real blank-field 350-μm source. The position and flux density of LOCK350.1 are RA = $10^{\rm h}52^{\rm m}43\overset{\rm s}{.}2$, Dec. = $57^\circ23'09''$ (J2000) and 32.8 $\pm$ 8.3 mJy. This position corresponds to a region of positive flux density in the 850-μm map and a 2.3σ peak is located $\simeq$4 arcsec from the position of LOCK350.1. There also appears to be a 4σ 1.4-GHz source and a faint 24-μm counterpart at these coordinates (Ivison et al. 2007; Biggs & Ivison 2006; see Fig. 2). This source is therefore probably the third secure 350-μm blank-field detection (see Khan et al. 2005 and Khan et al. 2007 for the first two).

[3] LOCK850.3 and LOCK850.14 are detected by Kovacs et al. (2006) but also discussed by Laurent et al. (2006).

[4] LOCK850.27 and LOCK850.76 were not previously associated with Bolocam sources, since they are new SHADES detections. LOCK850.27 and LOCK850.76 lie 4.8 and 10.6 arcsec away from two Bolocam sources, and so two new SCUBA/Bolocam associations are claimed here.

[5] A noise cut of 20 mJy was chosen arbitrarily, since higher S/N detections in noisier regions are more likely to be spurious; e.g. Coppin et al. (2005).

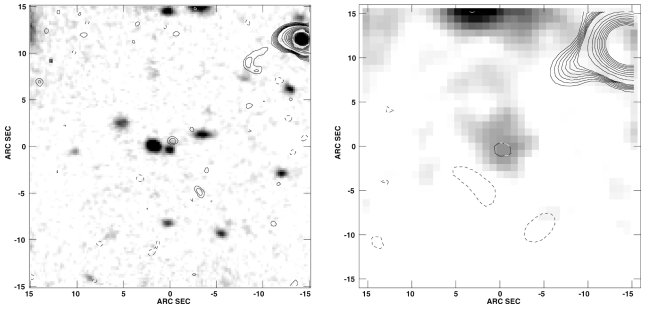

Figure 2. A multiwavelength view of LOCK350.1, a 3.9σ 350-μm blank-field source detected at RA = $10^{\rm h}52^{\rm m}43\overset{\rm s}{.}2$, Dec. = 57°23′9″ (J2000). The 30 × 30 arcsec^2 images are centred on the position of LOCK350.1. Left-hand panel: High-resolution (1.3 arcsec) 1.4-GHz contours ($-3, 3, 4, \ldots$,10, 20, $\ldots$,100 $\times\sigma$) from Biggs & Ivison (2006) overlaid on grey-scale archival *R*-band optical data. Right-hand panel: Low-resolution (4.2 arcsec) 1.4-GHz contours (-3, 3, 4, $\ldots$,10, 20, $\ldots$,100 $\times\sigma$) from Biggs & Ivison (2006) overlaid on grey-scale 24-μm data from Ivison et al. (2007).

4 ANALYSIS AND RESULTS

4.1 Constraints on the 350-μm source counts

We now attempt to crudely estimate the 350-μm source counts at our typical observed flux density, even though the SHARC-II data are not blank-field observations. We place an upper limit on the source counts using the number of detections acquired in the observed area; one would expect to do *worse* than this in a blank-field survey, since here known SMGs were observed. Given a total observed area of 48.3 arcmin^2 and seven detections above a 350-μm flux density of $\simeq$25 mJy, we estimate $N(>S) \lesssim 500\,\mathrm{deg}^{-2}$. We estimate a lower limit on the source counts by applying the SHARC-II detection rate of 850-μm sources to the whole SHADES area; one would expect to do at least as well in a blank-field search. We estimate a lower limit of $N(>S) \gtrsim 200\,\mathrm{deg}^{-2}$, given a SHARC-II detection success rate of 7/24 and a total of 120 SHADES sources found in $\simeq$720 arcmin^2. Note that we have neglected the possibility of enhanced density from clustering. The limits derived here are consistent with the predictions from Lagache et al. (2004) and scenario E from the semi-analytic models of Guiderdoni et al. (1998) (see Fig. 3). Although crude, this is the best available estimate of the 350-μm source counts at these flux densities. Khan et al. (2007) also report the 350-μm source counts above 13 mJy from a deep survey with SHARC-II. Large surveys planned with the Balloon-borne Large Aperture Subillimetre Telescope (BLAST; Devlin et al. 2004), *Herschel* (Pilbratt 2003), SCUBA-2 (Holland et al. 2006) and *Planck* (Tauber 2004) will be able to provide further constraints on the source counts at shorter submm wavelengths and over a wider dynamic range of flux densities.

4.2 SEDs of SMGs

The SEDs of SMGs is dominated by thermal emission from cold dust. SHARC-II photometry of the SHADES sources can determine the apparent temperature of the dust. In conjunction with knowledge of the redshift, this allows inference of dust masses, FIR luminosities and SFRs, allowing one to place these objects in context with other populations of high-redshift star-forming galaxies and AGN.

The shape of a luminous dusty galaxy SED is well approximated by a modified blackbody spectrum described by the dust temperature, $T_{\rm d}$, and dust emissivity $\epsilon \propto \nu^{\beta}$, where β lies in a physically

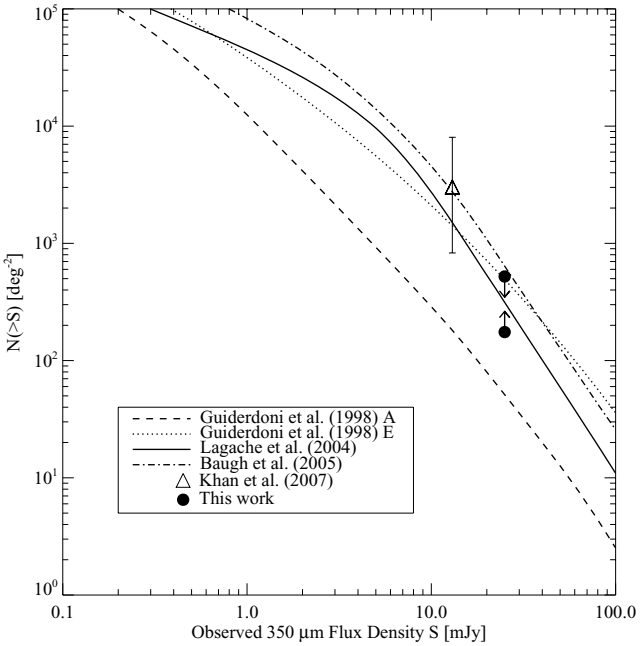

Figure 3. Cumulative 350-μm source counts. The solid line is a prediction of the source counts from Lagache et al. (2004) using a phenomenological model that constrains the IR luminosity function evolution with redshift. The dot–dashed line is the prediction of the 350-μm counts from the semi-analytic models of Baugh et al. (2005) which match the 850-μm number counts. The dotted and dashed lines are semi-analytic predictions of the source counts resulting from evolutionary scenarios E and A, respectively, from Guiderdoni et al. (1998), where star formation proceeds in 'burst' mode and includes either no ULIRGs (scenario A) or an increasing fraction of ULIRGs with redshift (scenario E). The solid circles with arrows are upper and lower limits on the source counts based on this work (see text) and are consistent with the source count predictions of Lagache et al. (2004) and scenario E of Guiderdoni et al. (1998). Scenario A of Guiderdoni et al. (1998) is inconsistent with the observational limits, as expected since it contains no ULIRGs. The source count constraint from Khan et al. (2007) above 13 mJy is also plotted (open triangle).

plausible range of 1–2 (Hildebrand 1983). There is a degeneracy between $T_{\rm d}$ and β which cannot be disentangled by our data (Blain et al. 2002), so we fix $\beta = 1.5$, which is consistent with the finding of Dunne & Eales (2001) for local galaxies and with the values obtained for carbonite and silicate grains from laboratory measurements (Agladze et al. 1994). This leaves two free parameters to be fitted: $T_{\rm d}$ and the SED normalization.

In practice we work in terms of the *apparent* dust temperature, $T_{\rm A} = T_{\rm d}/(1+z)$ and fit the data for each galaxy to $A\nu_{\rm obs}^{3+\beta}/[\exp(h\,\nu_{\rm obs}/kT_{\rm A}) - 1]$, where several factors of $(1+z)$ have been absorbed into the *apparent* normalization, A.

Assuming that the redshift is known, the rest-frame dust temperature can be recovered and the luminosity of the SMG can be determined by integrating the SED. In cases where the spectroscopic redshift is ambiguous, the most reliable or probable spectroscopic redshift available from the literature has been chosen and is listed in Table 5. For sources with only a 90 per cent confidence photometric redshift lower limit, the redshift is taken at this limit (see Table 4).

We characterize the shape of the SEDs independently of the photometric redshifts because we do not use the radio data in our fits to the SED, and where photometric redshifts are used they have been determined using all available FIR and radio photometry (except for the 350-μm data from this paper).

Table 5. Derived dust temperatures (T_d), FIR luminosities (L_{FIR}), illuminated dust masses (M_d) and SFRs for the 350-μm observed SHADES SMGs. The emissivity, β, is fixed at 1.5 and the best spectroscopic or photometric redshifts are used in fitting to the 350- and 850-μm photometry, plus 1.1- and 1.2-mm data if available. Errors in the fit parameters (i.e. the position of the peak and the SED normalization) are derived from the 68 per cent χ^2 confidence interval around the best-fitting values and have been carried through to all the derived quantities. Where appropriate, errors in the photometric redshifts have also been folded into the uncertainties.

SHADES ID	z	T_d (K)	L_{FIR} ($\times 10^{12}$ L$_\odot$)	M_d ($\times 10^9$ M$_\odot$)	SFR (M$_\odot$ yr^{-1})	Notes
With a spectroscopic redshift						
LOCK850.01	2.148	27^{+4}_{-3}	$2.3^{+1.0}_{-0.8}$	$1.4^{+0.6}_{-0.3}$	390^{+170}_{-130}	See Kovacs et al. (2006)
LOCK850.03	3.036	39^{+4}_{-4}	$9.6^{+3.5}_{-2.8}$	$0.8^{+0.2}_{-0.2}$	1600^{+600}_{-480}	See Kovacs et al. (2006)
LOCK850.04	0.526	13^{+2}_{-2}	$0.08^{+0.03}_{-0.03}$	$2.7^{+0.9}_{-0.6}$	13^{+6}_{-4}	
LOCK850.12	2.142	33^{+14}_{-12}	$3.2^{+8.2}_{-2.6}$	$0.7^{+1.4}_{-0.3}$	550^{+1400}_{-440}	See Kovacs et al. (2006)
LOCK850.14	2.611	39^{+7}_{-5}	$8.0^{+4.6}_{-2.8}$	$0.5^{+0.2}_{-0.1}$	1400^{+790}_{-480}	See Kovacs et al. (2006)
LOCK850.16	1.147	25^{+9}_{-7}	$0.8^{+1.6}_{-0.5}$	$0.9^{+0.8}_{-0.4}$	140^{+280}_{-90}	
LOCK850.18	1.956	18^{+5}_{-7}	$0.5^{+0.6}_{-0.4}$	$2.7^{+17.0}_{-1.3}$	90^{+100}_{-70}	See Kovacs et al. (2006)
LOCK850.30	2.689	76^{+103}_{-21}	$40.0^{+932.0}_{-26.0}$	$0.1^{+0.1}_{-0.1}$	$6900^{+160\,000}_{-4500}$	See Kovacs et al. (2006)
LOCK850.33	2.664	31^{+8}_{-13}	$1.9^{+2.1}_{-1.5}$	$0.5^{+2.1}_{-0.2}$	330^{+370}_{-270}	
LOCK850.41	0.689	12^{+4}_{-6}	$0.04^{+0.05}_{-0.03}$	$1.7^{+12.0}_{-0.8}$	7^{+9}_{-6}	See Kovacs et al. (2006)
With a photometric redshift						
LOCK850.02	$2.9^{+0.7}_{-0.1}$	30^{+12}_{-8}	$4.8^{+8.3}_{-2.9}$	$1.9^{+2.0}_{-1.0}$	830^{+1430}_{-490}	
LOCK850.06	$3.6^{+1.0}_{-0.1}$	55^{+51}_{-33}	$19.0^{+930.0}_{-19.0}$	$0.3^{+2.5}_{-0.2}$	$3300^{+160\,000}_{-3200}$	$\chi^2 \ll 1$
LOCK850.10	$3.1^{+0.9}_{-0.3}$	35^{+17}_{-10}	$5.3^{+4.5}_{-3.5}$	$0.9^{+1.2}_{-0.3}$	920^{+780}_{-610}	$\chi^2 \ll 1$
LOCK850.15	$2.4^{+0.4}_{-0.4}$	33^{+17}_{-29}	$4.0^{+37.0}_{-3.6}$	$1.5^{+9.0}_{-1.0}$	690^{+6400}_{-630}	
LOCK850.21	≥ 1.0	$>21^{+8}_{-7}$	$>0.3^{+0.6}_{-0.2}$	$>0.8^{+1.5}_{-0.4}$	$>60^{+100}_{-40}$	
LOCK850.22	≥ 2.0	$>19^{+10}_{-10}$	$>0.7^{+18.0}_{-0.7}$	$>2.9^{+49.0}_{-1.8}$	$>120^{+3000}_{-110}$	$\chi^2 \ll 1$
LOCK850.26	$3.6^{+0.1}_{-0.8}$	35^{+11}_{-15}	$3.8^{+30.0}_{-3.1}$	$0.5^{+1.7}_{-0.3}$	650^{+5200}_{-540}	$\chi^2 \ll 1$
LOCK850.27	$4.6^{+1.4}_{-0.4}$	27^{+22}_{-11}	$1.9^{+1.2}_{-1.2}$	$1.2^{+9.1}_{-1.0}$	330^{+1200}_{-210}	
LOCK850.28	≥ 2.0	$>29^{+7}_{-7}$	$>2.0^{+1.3}_{-1.3}$	$>0.9^{+0.9}_{-0.9}$	$>340^{+220}_{-220}$	$\chi^2 \ll 1$
LOCK850.47	≥ 1.5	$>27^{+19}_{-19}$	$>0.8^{+41.0}_{-0.8}$	$>0.5^{+37.0}_{-0.3}$	$>140^{+7100}_{-140}$	$\chi^2 \ll 1$
LOCK850.48	$2.4^{+0.5}_{-0.1}$	35^{+20}_{-12}	$2.6^{+9.4}_{-2.0}$	$0.5^{+0.8}_{-0.3}$	440^{+1600}_{-340}	
LOCK850.63	$2.6^{+0.4}_{-0.4}$	65^{+71}_{-59}	$22.0^{+2600.}_{-22.0}$	$0.1^{+850.0}_{-0.08}$	$3800^{+460\,000}_{-3800}$	$\chi^2 \ll 1$
LOCK850.64	≥ 1.5	$>22^{+8}_{-8}$	$>0.5^{+0.9}_{-0.4}$	$>1.3^{+2.8}_{-0.6}$	$>90^{+150}_{-70}$	
LOCK850.76	$4.6^{+1.4}_{-1.1}$	29^{+21}_{-19}	$2.4^{+2.1}_{-2.0}$	$0.9^{+100.0}_{-0.4}$	410^{+360}_{-350}	
LOCK850.77	$2.6^{+0.8}_{-0.1}$	92^{+140}_{-75}	$82.0^{+13\,000.0}_{-82.0}$	$0.06^{+0.6}_{-0.4}$	$14\,000^{+2300\,000}_{-14\,000}$	$\chi^2 \ll 1$, unphysical, misID?
SXDF850.1	$2.6^{+0.4}_{-0.3}$	25^{+10}_{-8}	$2.3^{+0.8}_{-1.8}$	$2.2^{+4.4}_{-1.2}$	400^{+130}_{-300}	$\chi^2 \ll 1$
SXDF850.3	$2.1^{+0.3}_{-0.1}$	27^{+10}_{-8}	$2.3^{+1.7}_{-1.6}$	$1.4^{+1.5}_{-0.6}$	400^{+300}_{-270}	$\chi^2 \ll 1$
SXDF850.8	$2.6^{+1.3}_{-0.1}$	30^{+11}_{-11}	$2.4^{+3.9}_{-2.0}$	$0.8^{+2.0}_{-0.4}$	410^{+680}_{-340}	$\chi^2 \ll 1$
SXDF850.11	$2.4^{+0.4}_{-0.4}$	46^{+29}_{-24}	$7.7^{+190.0}_{-7.3}$	$0.3^{+0.9}_{-0.1}$	$1300^{+32\,000}_{-1300}$	$\chi^2 \ll 1$
SXDF850.17	≥ 2.0	$>21^{+11}_{-11}$	$>0.9^{+23.0}_{-0.9}$	$>2.2^{+36.0}_{-1.4}$	$>160^{+3900}_{-150}$	$\chi^2 \ll 1$
SXDF850.119	$2.1^{+0.1}_{-0.1}$	29^{+15}_{-14}	$1.5^{+27.0}_{-1.4}$	$0.6^{+2.8}_{-0.3}$	260^{+4700}_{-240}	$\chi^2 \ll 1$

More complex SED modelling was not attempted (e.g. fitting two-temperature dust components as in Dunne & Eales 2001), since this would require more free parameters than can be constrained using the typically 2–3 photometric points which exist for each of our SMGs. The Wien side of the spectrum is sometimes also modified by a power law of the form $S_\nu \propto \nu^{-\alpha}$ to account for the increase in optical depth in this part of the spectrum and to provide a better fit to observational data (see Blain, Barnard & Chapman 2003). We neglect such elaborations here (see also Kovacs et al. 2006), since the Wien side of the spectrum is not sampled with our data. 24-μm photometry are available for SHADES sources but are complicated to interpret since this band samples polycyclic aromatic hydrocarbon and stellar emission features in high-redshift star-forming galaxies (e.g. Sajina, Lacy & Scott 2005).

The results of this fitting process are plotted in Fig. 4. Note that the 350-μm data point provides almost all of the constraining power on T_A.

We have measured the apparent temperatures (T_A) of an unbiased sample of SMGs from SHADES. We calculate the corresponding temperature distribution by adding a rectangle of area one centred on

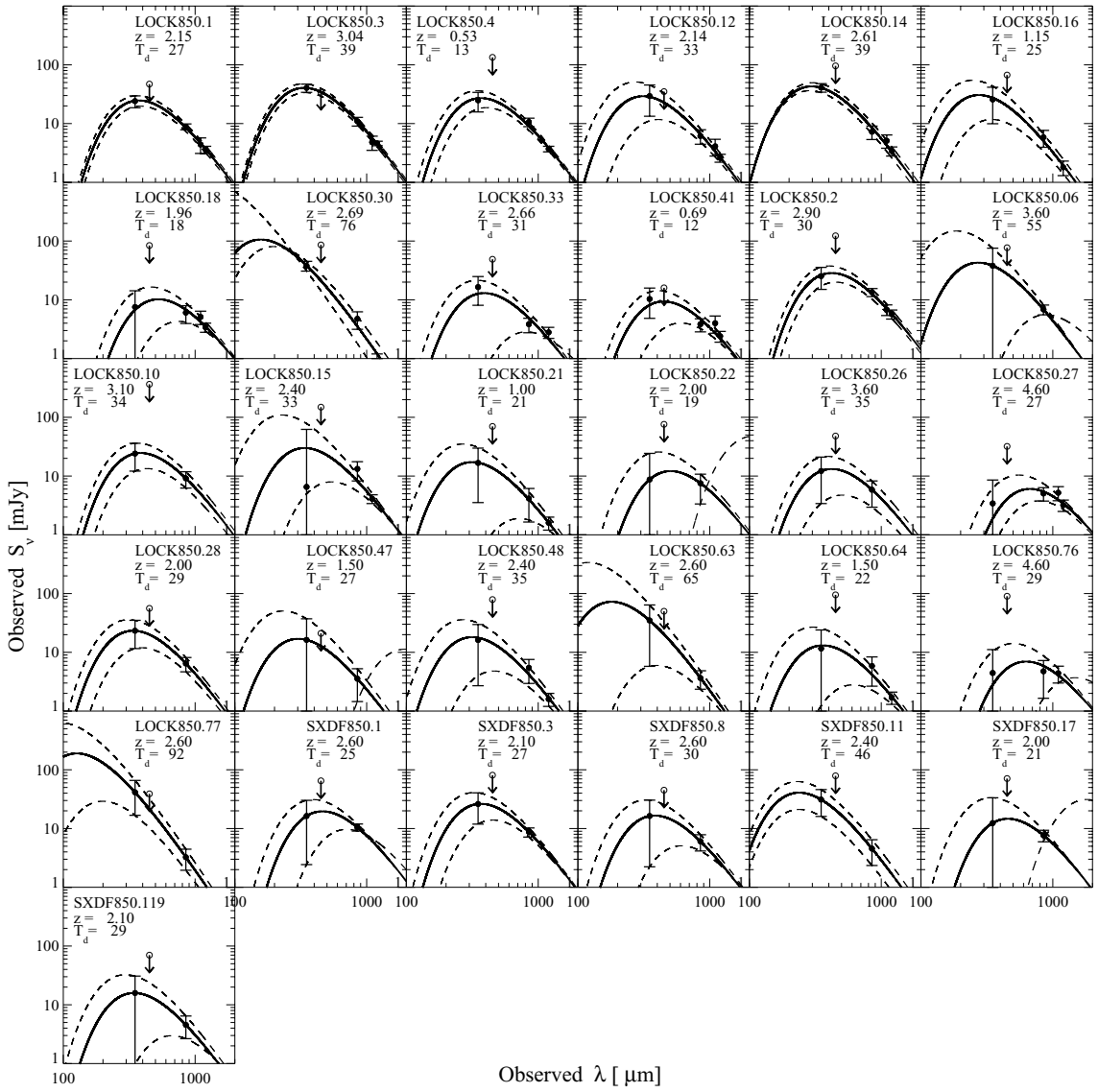

Figure 4. Best-fitting modified blackbody SEDs for SHADES 850-μm-selected SMGs with 350-μm photometry with β fixed to 1.5, in the same order as Table 5. The first 10 SEDs use the available spectroscopic redshifts, and the rest use only photometric redshift constraints. The dashed curves show the 1σ range in the best-fitting SED. The solid circles indicate photometry used to fit the SED, while the open circles show the SCUBA 450 μm upper limits which are not used explicitly in the fits (though they are never violated). The spectroscopic or photometric redshifts indicated in each panel have been used to recover the given rest-frame $T_{\rm d}$. Note that the 350-μm point provides almost all of the constraining power on the dust temperature.

the source $T_{\rm A}$, with a width given by the errors in $T_{\rm A}$ to the histogram (see Fig. 5). It appears that our survey selects SMGs with $T_{\rm A} \simeq (8 \pm 3)$ K. We recover the intrinsic dust temperature ($T_{\rm d}$) distribution of SMGs by shifting each SED into the rest frame, following a similar procedure to that described for the $T_{\rm A}$ distribution above (see Fig. 5). The $T_{\rm d}$ distribution appears to contain structure ('bumps' centred around 12, 28 and 35 K) and is broader compared with the $T_{\rm A}$ distribution. To investigate if this distribution is more structured and/or wider than we would expect by chance, we have simulated the temperature distribution we would expect to see if all SMGs have $T_{\rm d} = 28$ K. The simulated $T_{\rm d}$ distribution is constructed by adding an error box of area one centred on $T_{\rm d} = 28\,{\rm K} + {\rm rand} \times \sigma$, where 'rand' is a normally distributed random number, for each source. Although the shape and width of the simulated distribution changes notably depending on the random realization, we *never* reproduce the 'bumps' at $T_{\rm d} \simeq 12$ or 35 K and we *always* predict more SMGs at a few K than we see. Therefore we conclude that the underlying distribution is just a bit wider than we expect by chance and is consistent with most SMGs at 28 K with a few hotter ones. Now we compare the dust temperatures of our photometric and spectroscopic redshift subsamples and to previous estimates for SMGs.

We derive a mean $T_{\rm d} = (31 \pm 18)$ K (median $T_{\rm d} = 31$ K) for our sample of SMGs with spectroscopic redshifts. For the sample of 21 350-μm observed SMGs with only photometric redshifts, the mean is $T_{\rm d} = (35 \pm 17)$ K (median $T_{\rm d} = 29$ K). A two-sided Kolmogorov–Smirnov test reveals that the temperature distributions of the photometric redshift and spectroscopic redshift subsets are consistent with being drawn from the same distribution. Therefore we quote a mean $T_{\rm d} = (34 \pm 17)$ K (median $T_{\rm d} = 29$ K) for our entire sample of SMGs. Our mean $T_{\rm d}$ is consistent with previous estimates for SMGs from Chapman et al. (2005) ($T_{\rm d} = 36$ K for

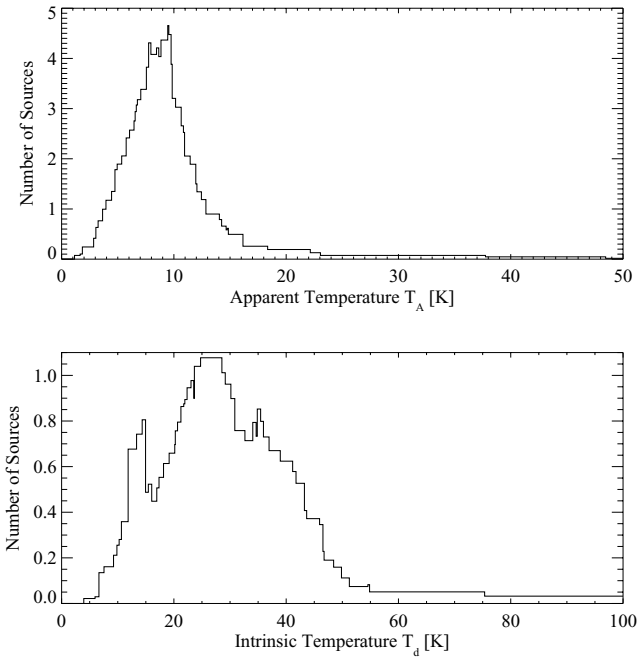

Figure 5. Apparent (observed) and rest-frame dust temperature distributions of an unbiased sample of SMGs. Each distribution has been calculated by adding a rectangle of area one centred on the source temperature (T_A or T_d), with a width given by the errors in the temperature (see Table 5) to the histogram. The T_A distribution reveals that our survey selects SMGs with $T_A \simeq (8 \pm 3)$ K. The T_d distribution contains bumpy features around 12, 28 and 35 K and is found to be broader than we would expect by chance (see text). The underlying distribution is consistent with most SMGs having $T_d \simeq 28$ K but with a few being a bit hotter ($\simeq$35 K).

radio-identified SMGs with spectroscopic redshifts), from Kovacs et al. (2006) ($T_d = 35$ K), and from Pope et al. (2006) ($T_d \simeq 30$ K for SMGs in the Great Observatories Origins Deep Survey-North, GOODS-N, region). In contrast, we find that the Farrah et al. (2003) ultraluminous infrared galaxy (ULIRG) sample has a median $T_d = 42$ K when their photometry are fit with our grey body (see also Clements et al. 2008). Thus SMGs appear to have lower temperatures on average than local ULIRGs, although bear in mind that local ULIRGs are selected at 60 μm which inherently introduces a bias to selecting hotter objects than submm observations would typically find.

The SED is integrated to estimate the bolometric luminosity of the SMG. Assuming that the FIR luminosity is predominantly powered by star formation (i.e. negligible contribution from an AGN), coming from a starburst of less than 100 Myr, with a Salpeter (1955) initial mass function, then the SFR can be calculated following Kennicutt (1998):

$$\mathrm{SFR}(\mathrm{M_\odot\,yr^{-1}}) = 1.7 \times 10^{-10}\, L_{\mathrm{FIR}}(\mathrm{L_\odot}). \quad (1)$$

The median FIR luminosity for our sample is $\simeq 2 \times 10^{12}\,\mathrm{L_\odot}$ (the mean is $\simeq 8 \times 10^{12}\,\mathrm{L_\odot}$, with a large scatter), which is consistent with what has been found previously for SMGs (e.g. Kovacs et al. 2006). The median SFR for the 350-μm observed SHADES sources is $\simeq$400 $\mathrm{M_\odot\,yr^{-1}}$, as calculated from equation (1). This is consistent with previous work, indicating that SMGs are significant contributors in the global star formation of the high-redshift universe (see e.g. Lilly et al. 1999; Blain et al. 2002; Chapman et al. 2005; Aretxaga et al. 2007).

We can also constrain the cold dust mass, M_d, in these obscured star-forming galaxies. The flux density of a galaxy at an observed frequency, ν_{obs}, is given by the usual relation (e.g. Hughes, Dunlop & Rawlings 1997)

$$S_{\nu_{\mathrm{obs}}} = B_{\nu'}(T)\kappa_{\nu'}\, M_d\,(1+z)/D_L^2, \quad (2)$$

where D_L is the cosmological luminosity distance and $B_{\nu'}$ is the Planck function evaluated at the emitted frequency, $\nu' = \nu_{\mathrm{obs}}(1+z)$. The quantity $\kappa_{\nu'}$ is the frequency-dependent mass-absorption coefficient (or 'effective area' for blackbody emission by a certain mass of dust) and $\kappa_{\nu'}$ can be extrapolated from an average $\kappa_{125\,\mu\mathrm{m}} = 2.64\,\mathrm{m^2\,kg^{-1}}$ assuming $\beta = 1.5$ (Dunne, Eales & Edmunds 2003).

Using equation (2), the median dust mass implied by the 850-μm observations is $9 \times 10^8\,\mathrm{M_\odot}$. Uncertainties in the dust masses are dominated by the uncertainty in the photometric redshifts (when these are used), T_d and the flux density at 850 μm. The uncertainty in $\kappa_{\nu'}$ is a factor of a few and has not been included in the dust mass error bars, but the relative dust masses in our sample will be correct if the same value holds for all SMGs (see Blain et al. 2002 and references therein for a discussion). Assuming that the maximum possible interstellar dust mass for a galaxy is about 1/500 of its total baryonic mass (see Edmunds & Eales 1998), the total baryonic mass of each SMG is estimated to be $M_{\mathrm{bary}} \simeq 5 \times 10^{11}\,\mathrm{M_\odot}$. For comparison, the baryonic mass of the Milky Way is about $10^{11}\,\mathrm{M_\odot}$.

The best-fitting SEDs are given in Fig. 4, while Table 5 gives the best-fitting value of T_d for each SMG, as well as the derived L_{FIR}, M_d and SFR.

Errors in the fit parameters (i.e. the position of the peak and the SED normalization) are derived from the 68 per cent χ^2 confidence interval around the best-fitting values. These errors have been carried through to all the other derived quantities in Table 5. Obviously, for galaxies with only two FIR photometric points, the SEDs are not well constrained and the minimum reduced χ^2 values are significantly less than one. Photometric redshift errors have been folded into the uncertainties for derived quantities. We assume that our adopted model (a grey body with $\beta = 1.5$) is correct and so the quoted errors do not include a contribution from possible systematic errors. Adopting a constant value of β is equivalent to assuming that the dust has similar properties in all galaxies. This is probably a reasonable assumption. As additional precise photometric data become available (from *Herschel* for example) β will be able to be constrained by direct fitting. Note, however, that changing the value of β by ± 0.5 (between physically plausible values) has the effect of changing the derived dust temperature by about $\pm$5–10 K, which in turn affects the derived luminosities of the SMGs by $\pm$20–40 per cent.

The SMG population is therefore confirmed to be dominated by massive ($>10^{12}\,\mathrm{M_\odot}$, assuming $M_{\mathrm{tot}}/M_{\mathrm{baryons}} \simeq 6$), luminous ($\simeq 2 \times 10^{12}\,\mathrm{L_\odot}$) star-forming (SFR $\simeq$400 $\mathrm{M_\odot\,yr^{-1}}$) galaxies with dust temperatures of $\simeq$35 K. In contrast, local starburst galaxies with similar temperatures (Dunne et al. 2000: $\bar{T}_d = 36$ K) are not usually classified as ULIRGs, since they are about 10 times less luminous ($L_{\mathrm{FIR}} \sim 10^{11}\,\mathrm{L_\odot}$). In addition, SMGs have more than 10 times more dust than local starburst galaxies, which could be explained by any of the following reasons: (1) SMGs are hosted in galaxies 10 times more massive than local starbursts; (2) SMGs are more gas- and dust-rich for a given baryonic mass, being at an earlier stage in evolution with a higher gas fraction or (3) the dust properties evolve with redshift and high-redshift dust has a higher emissivity and so produces more submm emission for a given mass of dust.

5 DISCUSSION

5.1 Trends in the data and consideration of selection effects

We first consider selection effects in our data before looking for trends in the derived properties. It is not surprising that the S_{350}/S_{850} colour appears to be independent of redshift (see Fig. 6), owing to the small dynamic range in flux densities of the 850-μm-selected sources. The colour could evolve with redshift, given a wider dynamic range. With this in mind, the relationship between dust temperature and redshift is examined in Fig. 7. Note that the spectroscopic and photometric redshift samples have about the same scatter and that the data deviate about the horizontal line in Fig. 7 (the sample median) by about ±5 K between redshifts of about 1 and 4 (except for a few outliers). It appears that the SMGs span a range of dust temperatures, with an apparent trend of T_d increasing with z. A Spearman rank test reveals a strong correlation in the data with spectroscopic redshifts and a weaker correlation when the photometric redshift sample is included. Is this due to selection effects or is this evidence for evolution of SMGs/ULIRGs with redshift?

In order to test for selection effects in our data, we populate the T_d–z parameter space of Fig. 7 by assuming reasonable distributions of SMG properties and apply 850- and 350-μm cuts to the data to see if the trends seen in Fig. 7 can be reproduced by selection effects alone. The dust temperature distribution of SMGs is assumed to be a simple Gaussian with a mean of 35 K and σ = 6 K, consistent with observations (e.g. Kovacs et al. 2006; Huynh et al. 2007). We create a $\beta = 1.5$ grey body SED with a temperature randomly selected from the temperature distribution, with a normalization constrained so that L_{FIR} is within the range of what we know about SMGs, i.e. a simple Gaussian distribution with a mean of $6.7 \times 10^{12}\,L_\odot$ and $\sigma = 3.0 \times 10^{12}\,L_\odot$ (e.g. Pope et al. 2005). A redshift for each source is randomly selected from a simple uniform redshift distribution spanning $0 \leq z \leq 5$ to allow observed 850- and 350-μm fluxes to be calculated. We reject an SMG from our surveyed sample if its 850- and 350-μm flux densities are less than 4 and 25 mJy, respectively. This procedure is repeated 100 times and the shaded region in Fig. 7 indicates the region where selection effects preclude the detection of SMGs in our 350-μm survey of 850-μm-selected SMGs. We miss sources in the lower right-hand region (high redshift, low temperature) of Fig. 7 because they are not bright enough at 850 μm to make it into our SHADES sample. In addition some of the 850-μm-selected sources are too faint at 350 μm. On the other hand, there seems to be a dearth of sources in the data at low redshifts with high dust temperatures (and consequently, high luminosities), where we are not prone to any selection effects (Fig. 7). The lack of sources in the upper left-hand part of Fig. 7 is probably a consequence of the long-established strong

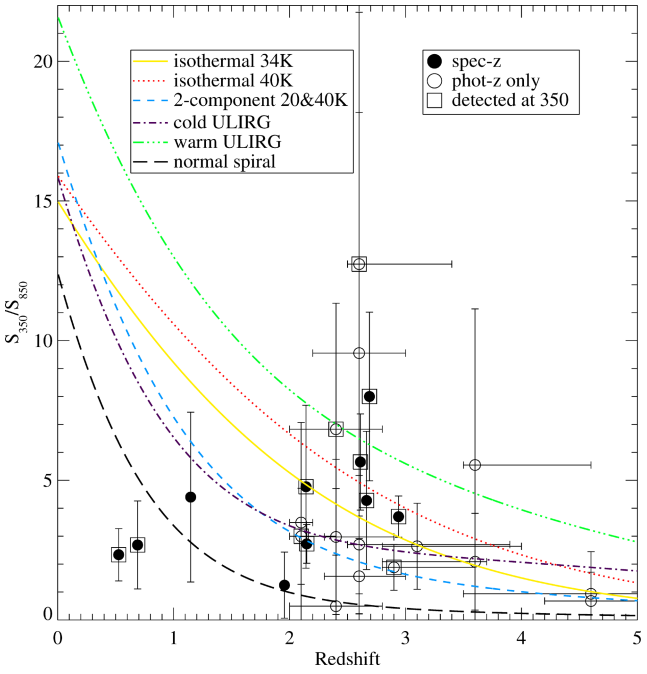

Figure 6. Observed S_{350}/S_{850} colour versus redshift using the values from Table 4. See inset for a description of the plot symbols. Sources with only redshift lower limits are omitted from this plot. The colour appears to be independent of redshift in these data (the median colour is 3.0), which is not surprising given the lack of dynamic range in the flux densities of the detected sources at 850 μm. Given a higher dynamic range in flux in future studies, we could attempt to trace SED evolution with redshift by distinguishing between models. We have plotted some plausible models including (see inset for legend) an isothermal grey body with $T_d = 40$ K, $\beta = 1.5$ (e.g. Blain et al. 2002); an isothermal grey body $T_d = 34$ K, $\beta = 1.5$ (this work); a two-component typical IR-bright starburst galaxy with T_d = 20 and 40 K, $\beta = 2$ and $M_{cold}/M_{warm} = 30$ (e.g. Dunne & Eales 2001); a theoretical warm ULIRG $T_d = 24$ and 50 K, $\beta = 2$ and $M_{cold}/M_{warm} = 5$; a normal spiral (e.g. Milky Way, NGC891 or M51) with $T_d = 15$ and 30 K, $\beta = 2$ and $M_{cold}/M_{warm} = 100$; a cold ULIRG (e.g. Arp220) with $T_d = 18$ and 48 K, $\beta = 2$ and $M_{cold}/M_{warm} = 42$.

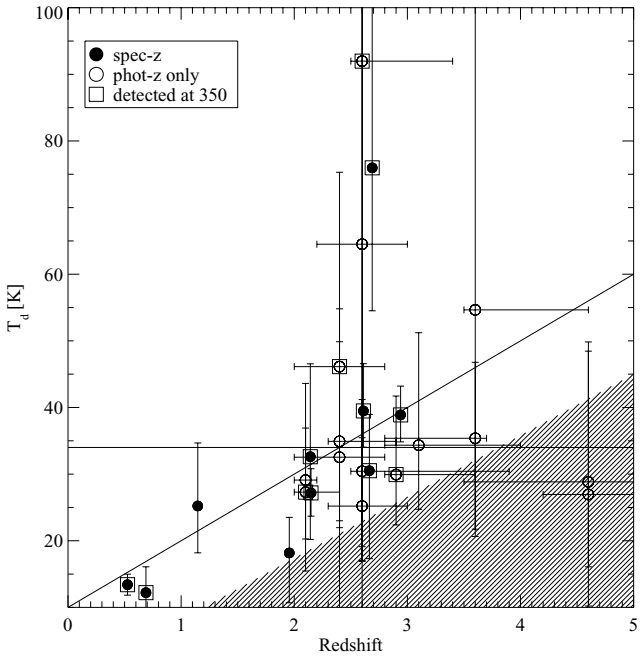

Figure 7. Derived dust temperature versus redshift for the sample of SMGs. See inset for a description of the plot symbols. The horizontal line represents the median dust temperature of the sample. The diagonal solid line indicates an observed dust temperature of 10 K, i.e. $T_d = 10(1 + z)$ K, and appears to fit the data better; a similar conclusion was also noted by Kovacs et al. (2006). This is not surprising, given that we find a constant S_{350}/S_{850} with redshift, as seen in Fig. 6. Combined with Monte Carlo simulations of the sample selection effects (see text), it appears that the absence of 30 K sources seen at $z \gtrsim 3$ is mainly due to a selection effect from SHARC-II, indicated by the shaded region. The lack of objects in the upper left-hand part is the result of evolution and shows that the 850-μm survey detects fewer warm SMGs in the low-redshift universe than at high redshift. See also Chapman et al. (2005).

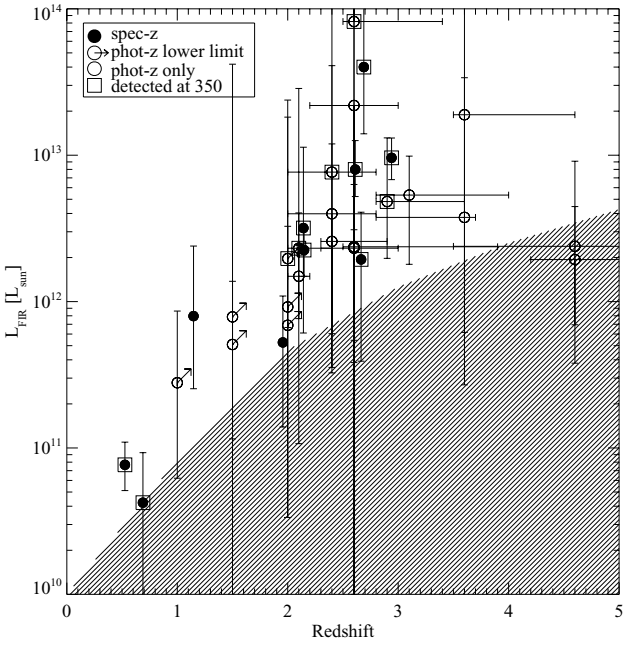

Figure 8. Bolometric luminosity versus redshift for the sample of SMGs. The plot symbols are the same as in Fig. 6, except that arrows now indicate points with redshift lower limits. The shaded region indicates selection effects from SHARC-II. There appears to be a dearth of higher luminosity sources at low redshift: a hint of strong luminosity evolution for SMGs with redshift.

luminosity evolution of the submm population (see fig. 2 in Smail, Ivison & Blain 1997), i.e. there are not as many sources at low redshift with temperatures $\gtrsim$35 K with sufficient luminosity to be detected by SHADES at 850 μm. Of course there could still be a systematic temperature dependence which might be seen by deep 450- and 850-μm SCUBA-2 data through the detection of many more 450-μm sources at fainter flux densities.

This idea can be further investigated when the relationship between $L_{\rm FIR}$ and redshift is examined (Fig. 8), since there is an intrinsic correlation between temperature and $L_{\rm FIR}$. As before, SHARC-II is insensitive to the shaded region in Fig. 8 (i.e. misses SMGs cooler than $T_{\rm d}/(1+z) \simeq 7$ K). Due to the increased volume at low redshifts, we would expect to see about two high-luminosity sources between redshifts of 0 and 1. Thus there appears to be a hint of a dearth of higher luminosity SMGs at the lowest redshifts compared to higher redshifts that cannot be explained by selection or volume effects.

These results are difficult to make sense of unless a strong SMG evolution with redshift is invoked. Millimetre-wave cameras such as MAMBO, Bolocam and AzTEC might be sensitive to cooler SEDs and could perhaps select SMGs to fill in this region of the ($L_{\rm FIR}, z$) plane. There also seems to be a lack of SMGs at low redshifts and high luminosity, indicating that SCUBA-selected SMGs are intrinsically more luminous at high redshifts. This is consistent with what was found by Ivison et al. (2002) and Pope et al. (2006) and suggests a strong evolution of SMGs/ULIRGs with redshift. Thus, Fig. 7 is just a reflection of the known effect seen in Fig. 8, i.e. that the most luminous SMGs are at higher redshifts. This means that they must be evolving very steeply with redshift (i.e. 'downsizing'). This idea has already been explored in Wall, Pope & Scott (2008). Larger samples of SMGs with robust redshifts and a wider dynamic range in 350- and 850-μm flux densities and luminosity are needed to test this idea further and to fully describe the evolution of the luminosity function of SMGs.

6 CONCLUSIONS

We have performed follow-up mapping at 350 μm using SHARC-II of several 850-μm-selected sources from SHADES. In total there are flux density measurements for about 25 per cent of the SHADES SMGs, of which this work has provided 21 new flux density constraints.

The combination of 350- and 850-μm, 1.1-, and/or 1.2-mm photometry and spectroscopic or photometric redshifts have provided estimates of $T_{\rm d}$ and $L_{\rm FIR}$ for each 350-μm-observed SHADES SMG by fitting a modified blackbody function to the data. The SMGs population is confirmed to be dominated by very dusty ($M_{\rm dust} \simeq 9 \times 10^8\,{\rm M}_\odot$), luminous ($L_{\rm FIR} \simeq 2 \times 10^{12}\,{\rm L}_\odot$) star-forming (SFR $\simeq 400\,{\rm M}_\odot\,{\rm yr}^{-1}$) galaxies with dust temperatures of $\simeq$35 K. We have measured the temperature distribution of SMGs and find that the underlying distribution is slightly broader than implied by the error bars, and that most SMGs are at 28 K with a few hotter.

With the data in hand, it is very difficult to understand whether we are just seeing a combination of selection effects and the known luminosity evolution of SMGs, or whether the SEDs might also systematically change with redshift. Larger samples of SMGs with a broader selection function will enable this to be fully investigated, e.g. with a deep 450-μm survey, a primary goal of the upcoming SCUBA-2 Cosmological Legacy Survey.[6]

Using these data, we have also been able to estimate the 350-μm source counts at $200\,{\rm deg}^{-2} \lesssim N(S \gtrsim 25\,{\rm mJy}) \lesssim 500\,{\rm deg}^{-2}$. Large blank-field surveys at 350 and/or 450 μm will allow us to study a statistically significant population of lower redshift and/or hotter dust temperature galaxies, responsible for emission nearer to the peak of the extragalactic background than those selected at 850 μm. These studies should provide a link between galaxies detected at ∼1 mm and those selected in the mid-IR with *Spitzer*. Such comparisons should allow us to investigate the evolution of FIR emitting galaxies and how they contribute to the background at different wavelengths.

ACKNOWLEDGMENTS

We thank Darren Dowell and Attila Kovacs at Caltech, who provided support and advice before, during, and after the CSO observing runs and to the CSO crew for support. The CSO is operated by Caltech under a contract from the National Science Foundation (NSF). KC, MH, AP and DS acknowledge support from the Natural Sciences and Engineering Research Council of Canada (NSERC). KC also acknowledges the Particle Physics Association Research Council (PPARC) for support. IS acknowledges support from the Royal Society. IA and DH acknowledge support from CONACyT grants. JW is grateful for support provided by the Max-Planck Society and the Alexander von Humboldt Foundation. EvK acknowledges support from FWF grant P18493.

REFERENCES

Agladze N. I., Sievers A. J., Jones S. A., Burlitch J. M., Beckwith S. V. W., 1994, Nat, 372, 243
Archibald E. N. et al., 2002, MNRAS, 336, 1
Aretxaga I. et al., 2007, MNRAS, 379, 1571
Baugh C. M., Lacey C. G., Frenk C. S., Granato G. L., Silva L., Bressan A., Benson A. J., Cole S., 2005, MNRAS, 356, 1191
Biggs A. D., Ivison R. J., 2006, MNRAS, 371, 963

[6] http://www.jach.hawaii.edu/JCMT/surveys/Cosmology.html.

Blain A. W., Smail I., Ivison R. J., Kneib J.-P., Frayer D. T., 2002, Phys. Rep., 369, 111
Blain A. W., Barnard V. E., Chapman S. C., 2003, MNRAS, 338, 733
Chapman S. C., Lewis G. F., Scott D., Borys C., Richards E., 2002, ApJ, 570, 557
Chapman S. C., Blain A. W., Ivison R. J., Smail I. R., 2003, Nat, 422, 695
Chapman S. C., Blain A. W., Smail I., Ivison R. J., 2005, ApJ, 622, 772
Clements D. et al. 2008, MNRAS, in press
Coppin K., Halpern M., Scott D., Borys C., Chapman S. C., 2005, MNRAS, 357, 1022
Coppin K. et al., 2006, MNRAS, 372, 1621
Devlin M. et al., 2004, in Zmvidzinas J., Holland W. S., Withington S., eds, SPIE Conf. Proc. Vol. 5498, Millimeter and Submillimeter Detectors for Astronomy II, SPIE, Bellingham WA, p. 42
Dowell C. D. et al., 2003, in Phillips T. G., Zmuidzinas J., eds, SPIE Conf. Proc. Vol. 4855, Millimeter and Submillimeter Detectors for Astronomy. SPIE, Bellingham WA, p. 73
Dunlop J. S., 2001, New Astron. Rev., 45, 609
Dunne L., Eales S., 2001, MNRAS, 327, 697
Dunne L., Eales S., Edmunds M., Ivison R., Alexander P., Clements D. L., 2000, MNRAS, 315, 115
Dunne L., Eales S., Edmunds M., 2003, MNRAS, 341, 589
Edmunds M. G., Eales S. A., 1998, MNRAS, 299, L29
Farrah D., Afonso J., Efstathiou A., Rowan-Robinson M., Fox M., Clements D., 2003, MNRAS, 343, 585
Greve T. R., Ivison R. J., Bertoldi F., Stevens J. A., Dunlop J. S., Lutz D., Carilli C. L., 2004, MNRAS, 354, 779
Guiderdoni B., Hivon E., Bouchet F. R., Maffei B., 1998, MNRAS, 295, 877
Hildebrand R. H., 1983, QJRAS, 24, 267
Holland W. S. et al., 1999, MNRAS, 303, 659
Holland W. S. et al., 2006, in Zmuidzinas J., Holland W. S., Withington S., Duncan W. D., eds, SPIE Conf. Proc. Vol. 6275, Millimeter and Submillimeter Detectors and Instrumentation III. SPIE, Bellingham WA, p. 45
Hughes D. H., Dunlop J. S., Rawlings S., 1997, MNRAS, 289, 766
Huynh M. T., Pope A., Frayer D. T., Scott D., 2007, ApJ, 659, 305
Ivison R. J., 2006, Conf. Proc. Sintra, preprint (astro-ph/0701453)
Ivison R. J. et al., 2002, MNRAS, 337, 1
Ivison R. J. et al., 2005, MNRAS, 364, 1025
Ivison R. J. et al., 2007, MNRAS, 380, 199
Kennicutt R. C., 1998, ARA&A, 36, 189
Khan S. et al., 2005, ApJ, 631, 9
Khan S. et al., 2007, ApJ, 665, 973
Kovacs A., 2006, PhD thesis, Caltech
Kovacs A., Chapman S. C., Dowell C. D., Blain A. W., Ivison R. J., Smail I., Phillips T. G., 2006, ApJ, 650, 592
Lagache G. et al., 2004, ApJS, 154, 112
Laurent G. T. et al., 2005, ApJ, 623, 742
Laurent G. T., Glenn J., Egami E., Rieke G. H., Ivison R. J., Yun M. S., Aguirre J. E., Maloney P. R., 2006, ApJ, 643, 38
Leong M. M., 2005, URSI Conf. Sec., J3-J10, 426
Lilly S. J., Eales S. A., Gear W. K. P., Hammer F., Le Fevre O., Crampton D., Bond R. J., Dunne L., 1999, ApJ, 518, 641
Mortier A. M. J. et al., 2005, MNRAS, 363, 563
Pilbratt G. L., 2003, in Mather J. C., ed., SPIE Conf. Proc. Vol. 4850, IR Space Telescopes and Instruments. SPIE, Bellingham WA, p. 586
Pope A., Borys C., Scott D., Conselice C., Dickinson M., Mobasher B., 2005, MNRAS, 358, 149
Pope A. et al., 2006, MNRAS, 370, 1185
Sajina A., Lacy M., Scott D., 2005, ApJ, 621, 256
Salpeter E. E., 1955, ApJ, 121, 161
Sanders D. B., Mirabel F., 1996, ARA&A, 34, 749
Smail I., Ivison R. J., Blain A. W., 1997, ApJ, 490, L5
Spergel D. N. et al., 2003, ApJS, 148, 175
Tauber J. A., 2004, Adv. Space Res., 34, 491
Wall J. V., Pope A., Scott D. S., 2008, MNRAS, 383, 435

APPENDIX A: EFFECTIVE EXPOSURE TIMES

When describing astronomical data, it is common and straightforward to give total observation times, or perhaps in chopped systems the total time *on source*. These times give an indication of the amount of effort expended to collect the data. However, because the atmosphere is far from transparent at submm wavelengths (even in the atmospheric windows) and the transmission is so weather dependent, the total exposure time does not give a good indication of data quality or expected noise level in the final output. It is more useful to refer to the *effective total exposure* which is the noise-squared weighted sum of exposure times referred to a completely transparent atmosphere.

The optical depth of the atmosphere in a given direction is determined from the wavelength dependent optical depth at zenith, τ_λ, and the cosecant of the zenith angle, θ, of observation, called the airmass, A. Thus, the strength of an observed astronomical flux density, S_o is

$$S_\mathrm{o} = S\,\mathrm{e}^{-\tau_\lambda(t)A(\theta)}. \tag{A1}$$

At 850 μm, the zenith optical depth, τ_{850}, ranges from, say, 0.16 in very good weather to 0.7 in bad weather, and the optical depth at 350 or 450 μm is typically seven times higher. The first step in combining data collected at different times of night with different values of τ_λ and A is to correct S_o for atmospheric absorption by multiplying by $\mathrm{e}^{\tau_\lambda A}$ (see Archibald et al. 2002).

After correcting for atmospheric transients, etc., but not opacity, the *output* noise at the detector is fairly independent of atmospheric opacity, at least for SCUBA operating on the James Clerk Maxwell Telescope on Mauna Kea at 450 and 850 μm, and for SHARC-II operating at 350 μm at the CSO also on Mauna Kea. Therefore, the *effective* noise of an observation is inflated exponentially in τ_λ and A. The sum

$$t_\mathrm{eff} = \sum \Delta t_\mathrm{o} \mathrm{e}^{2\,\tau_\lambda(t)A} \tag{A2}$$

is the integration time that would be required with a completely transparent atmosphere to get the same noise level as a given noise-squared weighted sum of observations, each of size Δt_o. We call this the *effective exposure time* and find that tracking this quantity during observations is an effective way to monitor experimental progress.

In practice, the optical depth as a function of time is obtained from automated measurements made at the CSO at 225 GHz every 10 min. The optical depths at submm wavelengths are very well correlated with these values and one multiplies $\tau_{225\,\mathrm{GHz}}$ by about 4 and 24 to get optical depths for SCUBA at 850 and 450 μm, respectively, and by 26 to get τ for SHARC-II at 350 μm (Archibald et al. 2002).

As a numerical example, observation of a source which rises through transit with an average airmass of 1.3 and $\tau_{225\,\mathrm{GHz}} = 0.05$ for 4-h results in effective exposure times of 2.4 h at 850 μm, 20.7 min at 450 μm with SCUBA, and 9.5 min with SHARC-II. The shorter effective times at shorter wavelengths are a consequence of the fact that the atmosphere is not very transparent at those wavelengths. This is why space experiments like *Herschel*-SPIRE and *BLAST* are useful even with comparatively small apertures, and why neither of those experiments carries an 850-μm channel. Experience has shown that effective exposures of between 500 and 600 s with SHARC-II are often sufficient to detect faint extragalactic high-redshift sources.

This paper has been typeset from a TEX/LATEX file prepared by the author.